

Article

Rainfall- and Irrigation-Induced Landslide Mechanisms in Loess Slopes: An Experimental Investigation in Lanzhou, China

Wei Liu ¹, Ruiqiang Bai ^{2,*}, Xinran Sun ¹, Fang Yang ¹, Weiji Zhai ³ and Xing Su ⁴¹ Institute of Transportation, Inner Mongolia University, Hohhot 010070, China; liuwei@imu.edu.cn (W.L.)² State Key Laboratory of Frozen Soil Engineering, Northwest Institute of Eco-Environment and Resources, Chinese Academy of Sciences, Lanzhou 730000, China³ Inner Mongolia Third Construction Engineering Co., Ltd., Hohhot 010051, China⁴ Institute of Geological Hazards Prevention, Gansu Academy of Sciences, Lanzhou 730000, China

* Correspondence: rqbai@lzb.ac.cn; Tel.: +86-152-9419-0376

Abstract: To reveal the mechanism of rainfall- and irrigation-induced landslides in loess slopes within cold regions, a series of tests on loess samples subjected to different permeability durations were conducted, and the effects of rainfall on several performance indicators, including the permeability coefficient, composition, microstructure, soil–water characteristic curve, and the shear strength of the loess, were investigated. The results show that the permeability coefficient of the loess decreased by 68% after permeability testing. With increased permeability duration, there is a marked decrease in total dissolved solids, sand particles, and clay particles, contrasted with an increase in silt particles. This dynamic alters the original soil structure and impacts the soil–water characteristic curve of the loess. Additionally, rainwater infiltration heightens the effective saturation of the loess, in turn diminishing the shear strength of the loess as effective saturation increases. This reduction in shear strength is further intensified with extended infiltration time (or rainfall duration). A landslide is triggered once the shear strength diminishes to the level of the geostatic stress of the loess slope, and the influence of the rainfall-induced loss of soil shear strength should be taken into account during slope stability analysis. This study enhances the understanding of the initiation mechanisms of rainfall-induced landslides in loess slopes.



Citation: Liu, W.; Bai, R.; Sun, X.; Yang, F.; Zhai, W.; Su, X. Rainfall- and Irrigation-Induced Landslide Mechanisms in Loess Slopes: An Experimental Investigation in Lanzhou, China. *Atmosphere* **2024**, *15*, 162. <https://doi.org/10.3390/atmos15020162>

Academic Editor: Alexey V. Eliseev

Received: 22 December 2023

Revised: 20 January 2024

Accepted: 23 January 2024

Published: 26 January 2024



Copyright: © 2024 by the authors. Licensee MDPI, Basel, Switzerland. This article is an open access article distributed under the terms and conditions of the Creative Commons Attribution (CC BY) license (<https://creativecommons.org/licenses/by/4.0/>).

Keywords: loess slope landslide; rainfall; permeability coefficient; soil structure; shear strength

1. Introduction

Landslides represent a significant natural hazard, and the progressive disaster mode of shallow landslides poses considerable risks to human life and properties [1,2]. Landslides are triggered by various factors, including seismic activity, rainfall, and irrigation, among others [3–7]. Earthquake-induced landslides, in particular, are typically rapid events, offering little to no time for survival [8,9]. Rainfall-induced landslides, on the other hand, are a global phenomenon [10,11]. They often transpire either during or after periods of rainfall. Collins and Znidarcic postulated that the formation of these landslides is a complex process involving rainwater seepage and a decrease in soil shear strength. Ering et al. [12] explored slope stability under transient seepage conditions, discovering the sensitivity to antecedent rainfall, with rainfall intensity and duration significantly impacting slope instability. Furthermore, heavy rainfall can elevate the water table, potentially triggering a landslide [13]. This rise in the water table increases the pore water pressure within the soil, reducing the soil's effective stresses, and decreasing the slope stability. Through the application of constant-shear-drained triaxial tests, Anderson and Sitar [14] simulated rainfall-induced landslides. Huang and Yuin [15] proposed an internal response-based rainfall criterion to predict slope instability under rainfall conditions, observing that instability often originates at the

slope's toe. Sorbino and Nicotera [16] further indicated that rainfall diminishes the matric suction and weakens the strength of the shallow soil layers.

Irrigation can also serve as a catalyst for landslides [17]. Wen and He [17] utilized the isotropically consolidated undrained triaxial test and the constant shear drained triaxial test to simulate the initiation of irrigation-induced landslides. Their research also encompassed an analysis of alterations to the chemical constituents and mineral compositions within the shear zones, providing crucial insights into the complex processes underpinning such events. Furthermore, it is important to note that seepage flow could potentially lead to erosion, further contributing to the destabilization of slopes. The moisture in the soil will cause changes in the chemical composition and mineral composition of the soil, and the increase in clay mineral content will reduce the sliding force and induce the occurrence of landslides. Irrigation can cause seepage flow, which in turn leads to erosion within the loess [18,19]. Howard and McLane [20] discovered that the actions of upslope seepage, local seepage, and gravity could alter the surface grains of non-cohesive sediment, further elucidating the complex dynamics at play. Fluvial transport plays a key role in controlling sapping erosion in non-cohesive soils. This erosion primarily occurs in the upstream narrow sapping zone due to increased seepage forces. The subsequent cutting action can trigger slope failures in the undermining zone, underscoring the intricate interplay between various natural forces and geological characteristics in the phenomenon of landslides. The seepage process of water in the slope will produce the infiltration force, which will have a strength deterioration effect on the shallow rock and soil mass of the landslide body, resulting in an increase in the sliding force.

Slope instability can manifest in the vadose zone of shallow soils under partially saturated conditions [21]. Lu and Godt [22] proposed a framework for evaluating slope stability under steady unsaturated seepage conditions, identifying that slope instability could occur above the water table. In this context, several studies have suggested a relationship between the shear strength of soil and factors such as matric suction or saturation [23–25]. Furthering this line of inquiry, Rahimi et al. [26] examined the impact of the soil–water characteristic curve, the saturated permeability coefficient, and the unsaturated permeability function on landslide stability during rainfall events. Their findings suggest that slope instability is intrinsically linked to the drainage characteristics of the slope. Therefore, understanding these complex relationships is pivotal in developing effective mitigation strategies for landslide prevention. The decreased strength of unsaturated soil caused by the decrease in suction stress is also an important reason for inducing landslides.

Landslides triggered by rainfall or irrigation are intrinsically linked to the seepage processes within the soil. Gui and Wu [27] utilized the constant-suction shearing test and the shearing-infiltration test to investigate the failure mechanism of slope soil under water infiltration conditions. Their findings suggested that water infiltration reduces the matric suction in the soil, leading to the formation of excess pore water pressure. They further observed that the failure of unsaturated soil could transpire under constant shear stress during infiltration. Consequently, excessive deformation and the wetting–softening of the soil emerge as the primary factors inducing slope failure during water infiltration. Indeed, soil shear strength is significantly influenced by seepage. However, limited research has been conducted to evaluate the strength of unsaturated soils under varying seepage durations. Several studies have explored the impact of exchanges between groundwater and surface water on sediment properties [28–31]. For instance, when rainfall or irrigation water flows on the surface, the underlying unsaturated soils may become saturated. Conversely, in arid regions, evaporation induced by the dry climate can cause saturated soils to become unsaturated. These dynamic processes underscore the intricate relationship between seepage, soil properties, and slope stability.

The shear strength of slope soils critically impacts the stability of landslides [32,33]. The rainfall threshold affects the final stability of the slope by affecting the internal water exchange of the landslide [34]. For example, rainfall has a great impact on soil moisture, and scholars have built geohazard models for disaster prevention work [35–38]. Previous

analyses suggest that soil components, permeability characteristics, and saturation levels can change during rainfall and irrigation, leading to degradation in the shear strength of slope soils. This can subsequently trigger landslides, particularly in loess slopes, whose mechanical properties are highly susceptible to drying–wetting cycles. However, there is a dearth of research focusing on the fluctuation in the grain size, structure, and soil–water characteristic curve of unsaturated slope soils during rainfall, and the mechanism underlying rainfall-induced landslides in loess slopes remains inadequately elucidated. In this study, the mechanism initiating landslides in loess slopes induced by rainfall was explored. The methodology commences with the simulation of rainfall via a penetration test, followed by a permeability test on loess under varying permeability durations to ascertain the permeability coefficient. Subsequently, this study examines the soil–water characteristic curve of the loess subjected to different permeability durations. Further, we investigate the effects of rainfall on the components and shear strength of the loess. This understanding can provide valuable insights into the initiation of loess landslides due to seepage, thereby contributing to the development of effective landslide prevention strategies.

The Loess Plateau in China is particularly susceptible to rainfall and irrigation, resulting in substantial economic losses. A case in point is the landslide that transpired in Jinzhou and Lanzhou, on 17 September 2007, triggered by heavy rainfall. The perennial irrigation of the woodland on the top of the hill also had an impact on the occurrence of the landslide. This landslide disrupted the primary transportation route between Lanzhou and Jiuzhou, inhibiting travel for several days and affecting approximately 50,000 people’s access to Lanzhou. Furthermore, the incident disrupted the normal operations of approximately 100 entities. After this landslide, the region experienced multiple landslides in 2013 and 2017, causing significant economic losses. It is imperative to investigate the mechanisms behind rainfall-induced landslides on loess slopes, as this research will facilitate the development of preventative measures and risk mitigation strategies.

2. Materials and Methods

This study utilizes the Shixiakou landslide, which occurred in Jiuzhou and Lanzhou, China, as a case study (Figure 1). The landslide spans 75 m in length and 95 m in width, with a height of 140 m. The average slope angle in the primary sliding direction was 45°. The landslide had an average thickness of 13 m and the backwall height ranged between 6–7 m. In total, a mass of $6.2 \times 10^4 \text{ m}^3$ slid onto Jiuzhou Road. The landslide occurred in a loess area, which belongs to the 5th terrace of the Yellow River in China. Rainfall in this area primarily occurs between July and September. The average annual rainfall in Shixiakou is 316.7 mm, while the annual mean evaporation is 1399 mm. Typically, the loess of the slope is in an unsaturated state, and the landslide in question occurred during a rainfall event. This case study provides an ideal opportunity to explore the dynamics of rainfall-induced landslides in loess slopes.

The soil samples utilized in this study were obtained from the back wall of the Shixiakou landslide. Sampling was conducted using cutting rings with a diameter of 61.8 mm and a height of 40 mm. Following sampling, the undisturbed samples were carefully packaged in plastic wrap. To prevent damage during transportation, buffer materials were employed to safeguard the samples. The fundamental properties of the loess are detailed in Table 1, while the grain size distribution is depicted in Figure 2. These data offer valuable insights into the mechanical and physical properties of the loess, which are essential for understanding the dynamics of the landslide event.

In this investigation, both permeability and pressure plate tests were conducted. Four sets of undisturbed loess samples, exhibiting similar properties, were selected for these tests (Table 2). In the permeability test, permeability durations of 5 d (L-5), 10 d (L-10), 15 d (L-15), and 20 d (L-20) were employed. Following the penetration test, samples (primarily formed after natural air drying and subsequently shaped using a ring knife) were used

for grain size distribution testing, scanning electron microscope testing, and soil–water characteristic curve testing. The samples used for the permeability test measured 40 mm in height and 61.8 mm in diameter, while those used for the soil–water retention characteristic test were 10 mm in height and 40 mm in diameter. This systematic approach allowed for a comprehensive evaluation of the loess mechanical and hydrological properties.

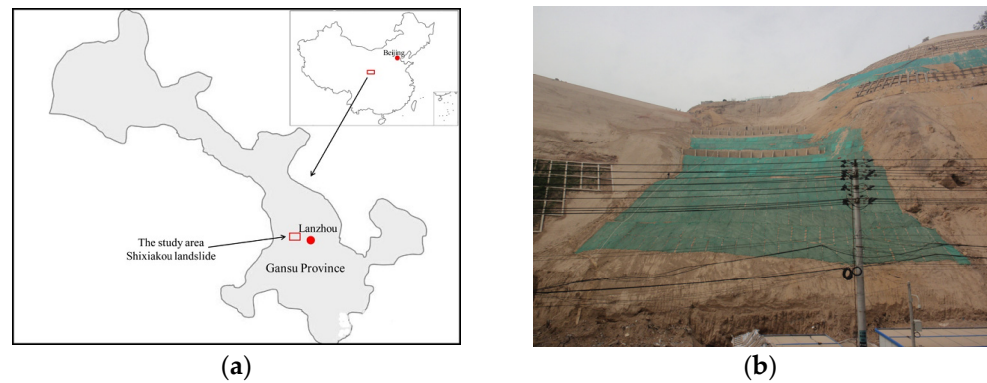


Figure 1. The Shixiakou landslide: (a) the location and (b) the landslide.

Table 1. Properties of the loess.

Density [g/cm ³]	Water Content [%]	Specific Gravity	Sand [%]	Silt [%]	Clay [%]	Plastic Limit [%]	Liquid Limit [%]
1.41	7.25	2.67	11.420	88.121	0.459	17.50	26.30

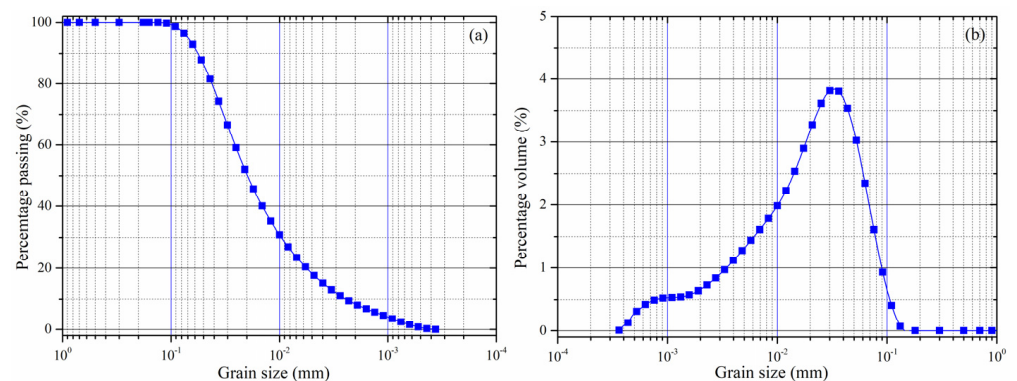


Figure 2. Grain size distribution of the loess: (a) percentage passing and (b) percentage volume.

Table 2. Test plan.

No.	Permeability Test (Y/N)	Pressure Plate Test (Y/N)	SEM Test (Y/N)
L-0	Y	Y	Y
L-5	Y	Y	Y
L-10	Y	Y	Y
L-15	Y	Y	Y
L-20	Y	Y	Y

The permeability test was conducted utilizing a TST-55 permeameter (Figure 3) in the Key Laboratory of Mechanics on Disaster and Environment in Western China. The TST-55 permeameter comprises a head tube, a penetration container (which consists of a cutting ring, permeable stone, sealing ring, upper plate, and lower plate), a water bottle, an exhaust pipe, and clips. This apparatus and its configuration ensured precise and reliable measurements of the permeability.



Figure 3. TST-55 Permeameter (Nanjing Zhongzhiyan Measurement and Control Technology Co., Ltd., Nanjing, China).

The pressure plate test was executed using a 1500 pressure plate extractor, manufactured by Soilmoisture Equipment Corp., Santa Barbara, CA, USA (Figure 4). This extractor includes a ceramic disk, a pressure chamber, and a drainage pipe. Ceramic disks with pressures of 5 bars and 15 bars were employed in the subsequent tests. The pressure plate test is founded on the axis translation technique. This technique implies that the water pressure has been translated upwards from the air pressure origin, moving away from the region of metastable states. This method allows for a precise measurement of soil–water retention characteristics under different pressures.



Figure 4. Pressure plate extractor.

In the permeability test, the initial step involved saturating the samples using a vacuum chamber and pump. The loess samples were required to remain in the vacuum chamber for a minimum of 24 h. Subsequently, the samples were placed in the penetration container, with petroleum jelly applied uniformly on the surface of the cutting rings. Next, filter paper, a permeable stone, and the top plate were positioned on the upper section of the penetration container. Simultaneously, filter paper, a permeable stone, and the lower plate were placed beneath the penetration container. The sealing rings were positioned between the top plate and the penetration container. The final preparatory stage involved filling the water bottle with distilled water, after which the test commenced. Prior to initiating the test, the exhaust work had to be considered to ensure the acquisition of accurate test data. A stopwatch was set in motion at the onset of the permeability test, and permeability data were collected throughout the testing process. Concurrently, a conduct meter was employed to assess the total dissolved solids (TDS) in the drained water during the testing phase.

In the pressure plate test, the samples were initially weighed using an electronic balance. Following this, the cutting rings were carefully positioned on the ceramic disk, and the sealing ring was placed between the top plate and the pressure chamber to apply pressure to the loess samples. Subsequently, the loess samples were weighed repeatedly until no water outflow from the ceramic disk was observed for a period of 3 d–5 d. Additional details regarding the use of a pressure plate extractor to acquire soil–water characteristic curve (SWCC) data can be found in the referenced literature [39–44]. Following the test, the grain size distributions of the samples were re-evaluated to analyze variations in the components during the tests. Concurrently, a scanning electron microscope test was conducted to analyze microstructural variations within the samples.

The permeability coefficient of the loess can be calculated using the formula [45],

$$K_T = 2.3 \frac{aL}{A(t_2 - t_1)} \lg \frac{H_1}{H_2} \quad (1)$$

where K_T symbolizes the permeability coefficient at temperature T °C, a represents the area of the head tube, L denotes the height of the loess samples, and A signifies the sample area. Additionally, t_1 and t_2 correspond to the start and end time, respectively, while H_1 and H_2 represent the initial and final head of the tube, respectively.

The VG model which is used to fit the SWCCs can be expressed as follows:

$$S_e = \frac{\theta - \theta_r}{\theta_s - \theta_r} = \left[\frac{1}{1 + (a\varphi)^n} \right]^m \quad (2)$$

where θ is the volumetric water content; S_e is the effective saturation; θ_s and θ_r are the saturated volume water content and residual volume water content; φ is the matric suction (kPa); and a , m , and n are the fitting parameters— a is related to the air entry value, m is related to the residual volume water content, and n is related to the overall slope of the soil–water characteristic curve.

To predict the shear strength in relation to soil suction, Vanapalli et al. [46] proposed a model, which can be expressed as follows:

$$\tau_f = c' + (\sigma - u_a) \tan \phi' + (u_a - u_w) S_e \tan \phi' \quad (3)$$

where τ_f is the shear strength of unsaturated soils; $u_a - u_w$ is the matric suction; c' and ϕ' are the effective shear strength parameters; $\sigma - u_a$ is the net normal stress; σ is the total normal stress; u_a is the pore air pressure; and u_w is the pore water pressure.

3. Results

3.1. Variation in the Permeability Coefficient

Figure 5 illustrates the temporal variation in the permeability coefficient of loess. It can be seen in Figure 5 that the permeability coefficient of the loess is approximately 1.5×10^{-5} cm/s after 1 d. All samples demonstrated a decrease in permeability coefficients over time, and the decrease rates gradually diminished. After a certain time, the permeability coefficients of the samples progressively stabilized. The reduction in permeability coefficient is intimately linked to the alteration in the pore structure of loess. As infiltration progresses, the structure of the undisturbed loess gradually deteriorates. This leads to a decrease in the large pores of soil, while the quantity of small and medium pores incrementally increases, resulting in a deterioration in pore connectivity and a subsequent decrease in the soil permeability coefficient. After the complete structural disruption of the undisturbed loess by infiltration, the permeability coefficients of the loess gradually stay stable, as the properties of the loess remain constant. This suggests that the permeability coefficient of the undisturbed loess is primarily influenced by its structure.

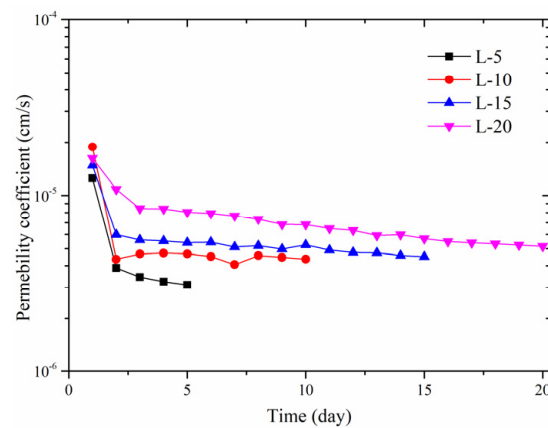


Figure 5. Permeability coefficient of the loess.

To further analyze the influence of infiltration on the loess permeability coefficient, Figure 6 shows the permeability coefficient losses of all of the tested samples. Figure 6 reveals that the absolute loss in the loess permeability coefficient is approximately 1×10^{-5} cm/s, and all of the relative permeability coefficient losses exceed 68%. These findings highlight that infiltration significantly diminishes the permeability attributes of the loess, subsequently inhibiting rapid drainage of infiltrated water from the soil. This process augments the soil weight and reduces the internal friction angle of the loess, thereby escalating the risk of landslides.

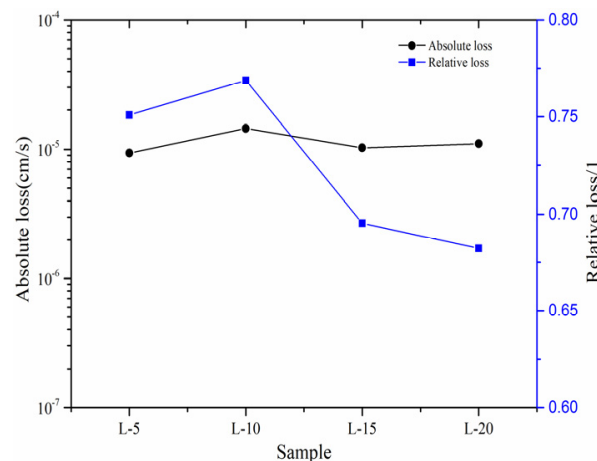


Figure 6. Permeability coefficient losses after the tests.

3.2. Composition Changes of the Loess during the Tests

To delve deeper into the compositional changes of loess during seepage, we evaluated the total dissolved solids (TDS) in the drained water and the grain size distributions of the loess after the tests. Figure 7 shows the temporal variations in TDS in the drained water, as measured by a conductivity meter. This indicates a rapid decrease in TDS over time, stabilizing after 5 d of seepage, suggesting that the salt content (dissolved solids) in the loess has reached a state of equilibrium. During the permeability test, the soluble salt content in the loess progressively decreased throughout the seepage process, damaging the salt cementation between soil particles. This process altered the particle contact mode and led to the restructuring of the pore structure. This restructuring process, characterized by a reduction in large pores and an increase in small and medium pores, continuously decreased the permeability coefficients of the soil samples. After 5 d of seepage, both the TDS and permeability coefficients appear to achieve stability.

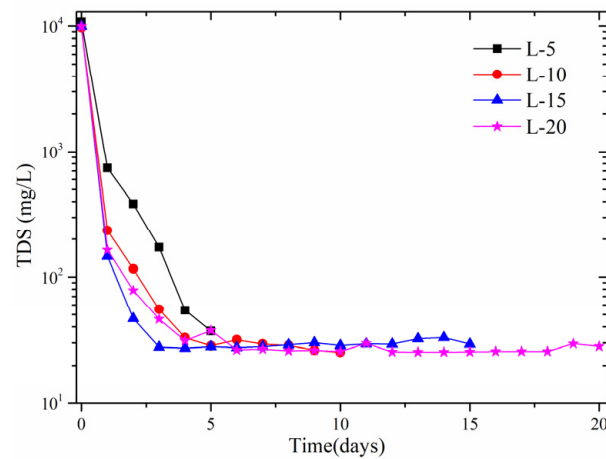


Figure 7. TDS variations of the loess samples under different seepage durations.

Figure 8 illustrates the grain size distributions of loess before and after the tests. It can be observed in Figure 8 that the content of particles with a grain diameter less than 0.01 mm diminishes after the test. Conversely, the content of soil particles with diameters ranging from 0.01–0.1 mm increases after the test. Moreover, soil particles with diameters less than 0.1 mm decrease in content after seepage. Macro voids and vertical joints present in the loess facilitate water infiltration. As water permeates the loess, clay particles are washed away, reducing the content of smaller soil particles. Concurrently, wetting-induced collapse of sand particles further reduces the clay particle content. This decline in clay particles weakens the clay particle cement, contributing significantly to loess degradation. Alterations in the contact mode and pore structure observed during the tests result in a reduced permeability coefficient. Subsequently, soil particles reorganize into a new, stable structure, corresponding to the stabilization phase of the permeability coefficient.

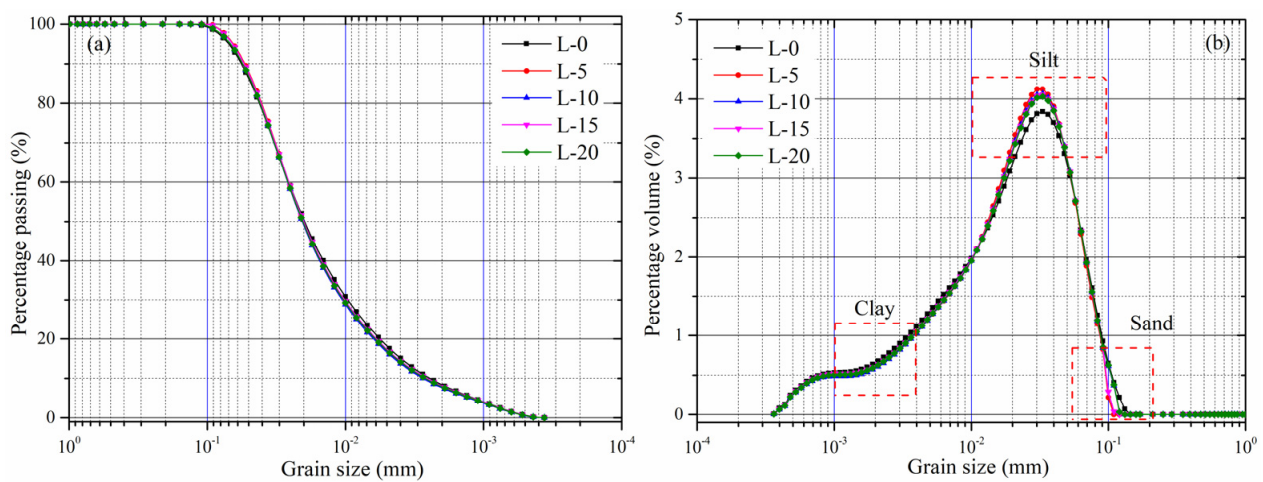


Figure 8. Grain size distributions of the loess after and before the tests: (a) percentage passing and (b) percentage volume.

Figure 9 presents electron microscopy images of the loess subjected to varying durations of infiltration. These images reveal the formation of large pores in the loess subsequent to the permeability tests, indicative of a new structural formation within the loess. The soluble salts within the loess progressively dissolve, and infiltrated water washes away some clay particles. Wetting-induced collapse of sand particles disrupts the original structure, culminating in the formation of a new structure.

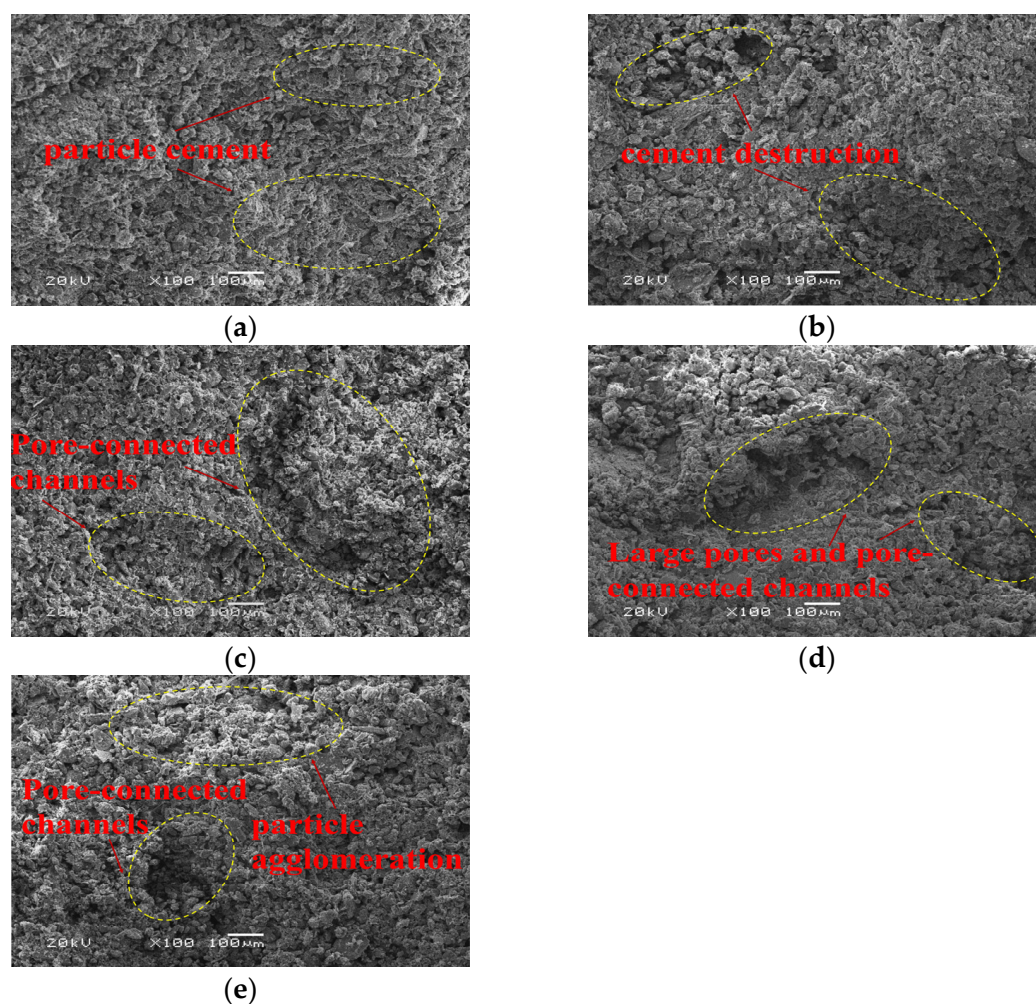


Figure 9. The electron microscopy images of the loess. (a) L-0. (b) L-5. (c) L-10. (d) L-15. (e) L-20.

3.3. Soil–Water Characteristic Curve

Figure 10 presents the relationship between the suction and water content of the loess. Initial observations suggest that the water content remains constant at the initial stage, subsequently declining as suction increases until it eventually aligns with the residual volume water content. Several mathematical models, such as those proposed by van Genuchten [47] and Fredlund and Xing [48], have been introduced to delineate the relationship between soil suction and water content. The van Genuchten model was employed to fit the test results to analyze the influence of seepage duration on the loess.

The pressure plate test was conducted within the range of 0–1500 kPa. Consequently, matric suction less than 1500 kPa was used to align with the van Genuchten model. The fitting parameters and their corresponding coefficients are shown in Table 2. They indicate an optimal fit with the van Genuchten model. This allows for an examination of the impact of seepage duration on the soil–water characteristic curve of the loess by analyzing the fitting parameters.

From Table 3, it can be seen that the saturated water content (θ_s) diminishes with the duration of seepage, suggesting that the porosity of the loess concurrently declines, a finding consistent with the alterations observed in pore structure induced by seepage. Moreover, the variables a and n also exhibit a reduction with seepage duration, implying a decrease in both the air entry value and the overall slope of the soil–water characteristic curve over the seepage period. Conversely, the variable m increases with the duration of seepage, corresponding to the fluctuation in the residual volume water content.

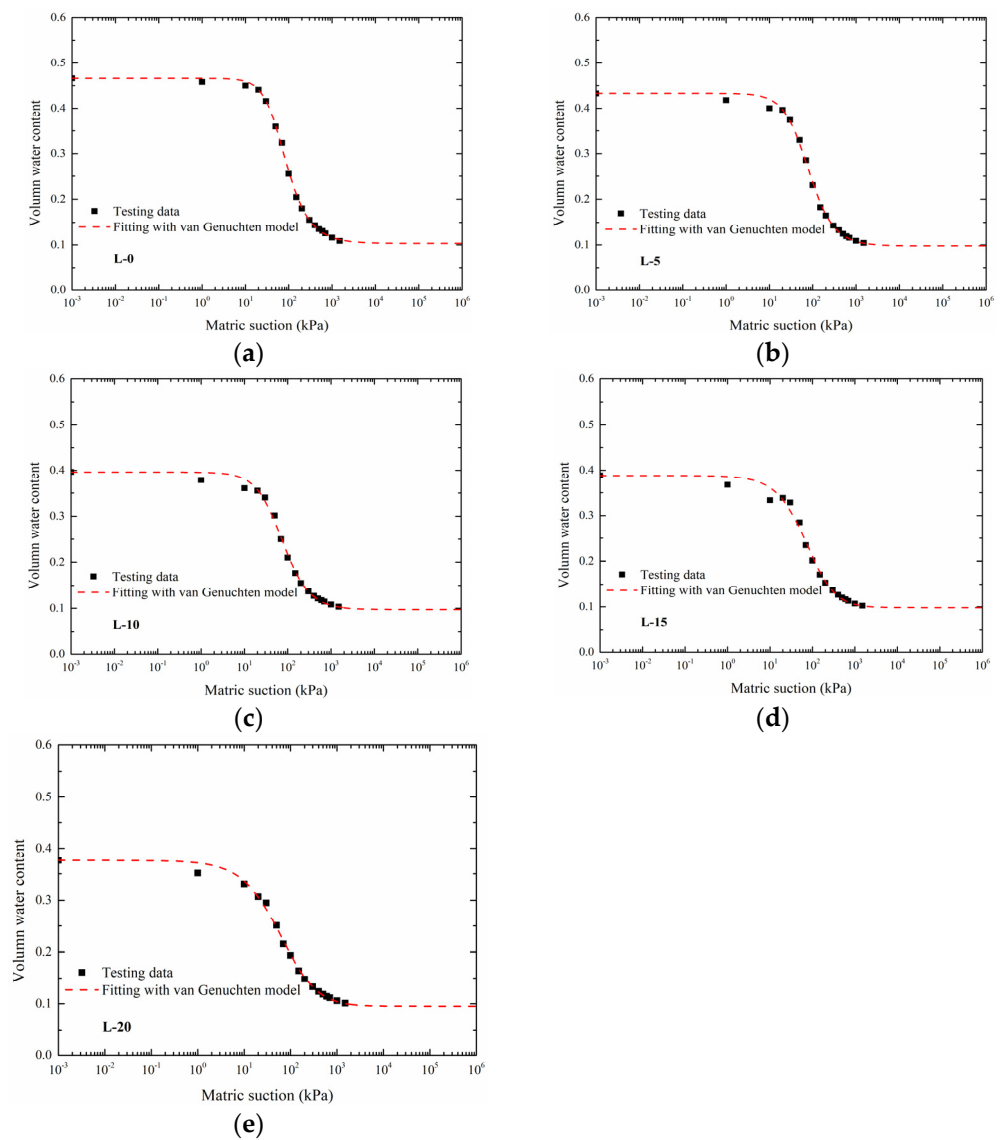


Figure 10. The relationship between the matric suction and water content of the loess under different seepage durations. (a) L-0. (b) L-5. (c) L-10. (d) L-15. (e) L-20.

Table 3. Fitting parameters.

Fitting Parameters	Samples				
	L-0	L-5	L-10	L-15	L-20
θ_s	0.466	0.433	0.396	0.388	0.376
θ_r	0.103	0.098	0.097	0.098	0.095
a	0.018	0.015	0.013	0.009	0.007
m	0.565	0.810	0.880	1.404	1.488
n	2.007	1.599	1.464	1.129	0.965
R^2	0.999	0.996	0.994	0.988	0.995

4. Discussion

In the study area, annual precipitation is low (average annual rainfall is 327 mm), necessitating irrigation for the vegetation, including trees and grass, before the onset of the rainy season. Commencing in March each year, farmers initiate the irrigation of trees at the slope apex. The irrigation water infiltrates the loess. Rainfall further contributes

to rainwater infiltration. Given the arid climate of Lanzhou, Gansu Province, China, evaporation rates are substantial, averaging approximately 1399 mm in the area. This results in drying–wetting cycles within the slope loess. These cycles induce changes in the loess properties, most notably its shear strength, which plays a pivotal role in determining slope stability.

The effective shear strength parameters, derived from triaxial tests ($c' = 21.5$ kPa and $\varphi' = 16^\circ$), are employed to predict the shear strength of unsaturated loess. A case study where the net stress equals 100 kPa is examined, and the variations in shear strength under different drying–wetting conditions are depicted in Figure 11. The shear strength envelopes of the loess exhibit nonlinearity, corroborating the findings of Fredlund et al. [49] and Cokca and Tilgen [50]. The shear strength of unsaturated loess was found to significantly increase with soil matric suction, albeit at a diminishing rate. Moreover, shear strength was observed to decrease with the duration of permeability.

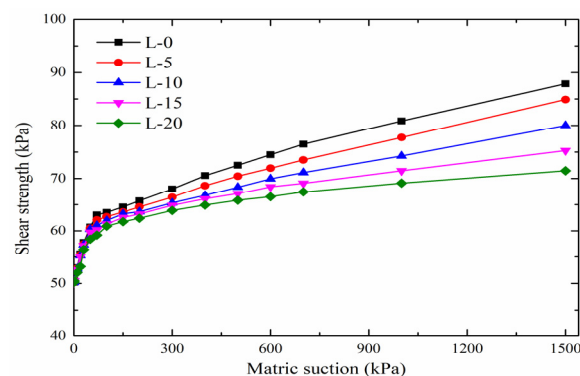


Figure 11. The shear strengths of the loess.

To further analyze the influences of permeability duration and saturation on the loess shear strength, we present the shear strength losses for all samples after the tests in Figure 12. From Figure 12a, it can be seen that the shear strength loss is zero in a saturation condition under varying permeability durations. However, under unsaturated conditions, there is a significant loss of shear strength, with the maximum loss reaching up to 18.68%. As shown in Figure 12b, a notable shear strength loss is evident during the wetting process, with the maximum loss at 42.90%. These findings reveal the significant role of both permeability duration and saturation in determining the loess shear strength, with saturation exerting a more profound influence than permeability duration. During rainfall, the infiltrating rainwater augments the soil saturation, leading to a decrease in soil shear strength as saturation increases. Moreover, the shear strength continues to decline with prolonged infiltration time (or rainfall duration). A landslide is triggered when the shear strength decreases to the level of the gravity stress of the soil slope.

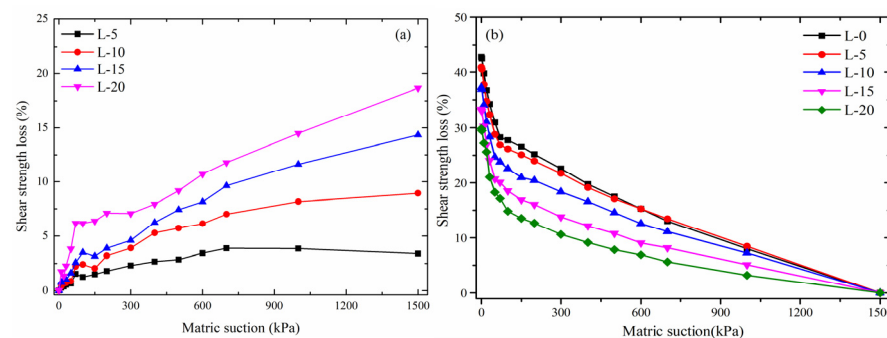


Figure 12. The shear strength losses of the samples: (a) the shear strength loss under different permeability durations and (b) the shear strength loss during the wetting process.

Based on the analyses above, the mechanism of the landslide can be revealed as shown in Figure 13. The loess within the shear zone commences wetting under rainfall. Soluble salts and clay particles within the loess decrease due to irrigation or rainfall, leading to alterations in soil particle contact mode and pore structure. This results in a decrease in larger pores and an increase in small- to medium-sized pores, consequently reducing the loess permeability properties. The infiltrated water cannot drain rapidly from the soil, thereby increasing the weight and decreasing the internal friction angle of the loess. Concurrently, the loess within the shear zone softens or weakens, and its shear strength significantly reduces due to wetting. After irrigation or rainfall, the infiltrated water rapidly evaporates due to the arid climate, initiating the drying of the loess within the shear zone. Nevertheless, the shear strength of the loess within the shear zone remains weaker than before. Upon subsequent wetting by the second or third irrigation or rainfall, the shear strength reduces more rapidly than the first instance. A landslide on the loess slope is triggered once the gravity stress exceeds the loess shear strength.

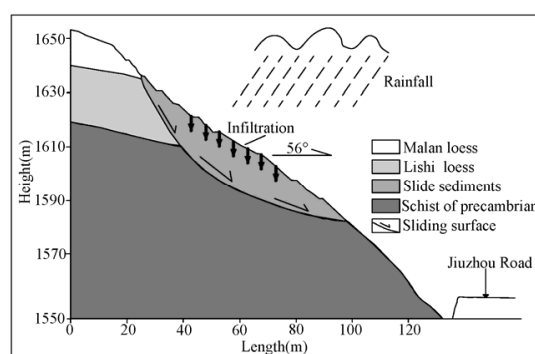


Figure 13. Initiation mechanism of the landslide for the loess slopes induced by rainfall.

5. Conclusions

To reveal the initiation mechanism of the landslide for the loess slope induced by rainfall, we carried out a series of tests for loess under different permeability durations and studied the influences of rainfall on the permeability coefficient, components, microstructure, soil–water characteristic curve, and the shear strength of the loess. The following conclusions can be made:

- (1) Infiltration significantly decreases the permeability properties of the loess, with a loss of over 68% of the permeability coefficient observed after the 5 d permeability test. Due to the reduced permeability coefficient, the infiltrated water cannot drain rapidly from the soil. The trapped water increases the weight and decreases the internal friction angle of the loess, thereby escalating the risk of landslides.
- (2) Seepage results in a decrease in total dissolved solids, sand particles, and clay particles, while silt particles increase. This alters the structure and impacts the soil–water characteristic curve of the loess. Consequently, the shear strength of the loess slope is also affected.
- (3) Infiltrated rainwater enhances soil saturation, leading to a decrease in soil shear strength as saturation increases. This shear strength continues to diminish with prolonged infiltration time (or rainfall duration). A landslide is initiated once the shear strength is reduced to the gravity stress of the soil slope. The loss of soil shear strength induced by rainfall must be factored into any slope stability analysis, particularly when dealing with a loess slope.

Author Contributions: Methodology, W.L. and F.Y.; validation, R.B.; formal analysis, X.S. (Xinran Sun), W.Z. and X.S. (Xing Su); investigation, X.S. (Xinran Sun); data curation, W.L. and F.Y.; writing—original draft preparation, W.L.; writing—review and editing, R.B.; funding acquisition, W.L., R.B. and X.S. (Xing Su). All authors have read and agreed to the published version of the manuscript.

Funding: This research was funded by the National Natural Science Foundation of China (Grant No. 42201142, 42101140, 42067066).

Institutional Review Board Statement: Not applicable.

Informed Consent Statement: Not applicable.

Data Availability Statement: The data presented in this study are available on request from the corresponding author. The data are not publicly available due to confidentiality of test data.

Acknowledgments: We thank Wang Juan and Xu He (Lanzhou University) for their useful suggestions.

Conflicts of Interest: Author Weiji Zhai is employed by the company Inner Mongolia Third Construction Engineering Co., Ltd. The paper reflects the views of the scientists and not the company. The authors declare no conflicts of interest.

References

- Troncone, A.; Pugliese, L.; Parise, A.; Conte, E. A practical approach for predicting landslide retrogression and run-out distances in sensitive clays. *Eng. Geol.* **2023**, *326*, 107313. [\[CrossRef\]](#)
- Giarola, A.; Bordoni, M.; Zucca, F.; Meisina, C. Analysis of the Role of Precipitation and Land Use on the Size of the Source Area of Shallow Landslides. *Water* **2023**, *15*, 3340. [\[CrossRef\]](#)
- Garciaurquia, E. Establishing Rainfall Frequency Contour Lines as Thresholds for Tainfall-induced Landslides in Tegucigalpa, Honduras, 1980–2005. *Nat. Hazards* **2016**, *82*, 2107–2132. [\[CrossRef\]](#)
- Xu, X.Q.; Su, L.J.; Liu, C. The Spatial Distribution Characteristics of Shallow Fissures of a Landslide in the Wenchuan Earthquake Area. *J. Mt. Sci.* **2016**, *13*, 1544–1557. [\[CrossRef\]](#)
- Hughes, F.E.; Madabhushi, S.P.G. Liquefaction Induced Displacement and Rotation of Structures with Wide Basements. *Soil Dyn. Earthq. Eng.* **2019**, *120*, 75–84. [\[CrossRef\]](#)
- Karakan, E.; Tanrinian, N.; Sezer, A. Cyclic Undrained Behavior and Post Liquefaction Settlement of a Nonplastic Silt. *Soil Dyn. Earthq. Eng.* **2019**, *120*, 214–227. [\[CrossRef\]](#)
- Tasiopoulou, P.; Giannakou, A.; Chacko, J.; Wit, S. Liquefaction Triggering and Post-liquefaction Deformation of Laminated Deposits. *Soil Dyn. Earthq. Eng.* **2019**, *124*, 330–344. [\[CrossRef\]](#)
- Yan, Z.; Du, X.; Fan, X. Parallel Numerical Analysis of the Failure Characteristics of Earthquake-induced Landslides. *Geosci. J.* **2015**, *4*, 529–538. [\[CrossRef\]](#)
- Robinson, T.R.; Davies, T.R.H.; Wilson, T.M.; Orchiston, C. Coseismic Landsliding Estimates for an Alpine Fault Earthquake and the Consequences for Erosion of the Southern Alps, New Zealand. *Geomorphology* **2016**, *263*, 71–86. [\[CrossRef\]](#)
- Fourie, A.B. Predicting Rainfall-induced Slope Instability. *Geotech. Eng.* **1996**, *119*, 211–218. [\[CrossRef\]](#)
- Lim, T.; Chang, M.; Vachon, B.L.; Abdolazadeh, A.M.; Cabral, A.R.; Lade, P.V.; Yamamuro, J.A.; Santoso, V.; Ng, Y.; Tam, C.; et al. Effect of Rainfall on Matric Suctions in a Residual Soil Slope. *Can. Geotech. J.* **1996**, *33*, 618–628. [\[CrossRef\]](#)
- Ering, P.; Babu, G.L.S. Probabilistic Back Analysis of Rainfall Induced Landslide—A Case Study of Malin Landslide, India. *Eng. Geol.* **2016**, *208*, 154–164. [\[CrossRef\]](#)
- Rahardjo, H.; Lim, T.; Chang, M.; Fredlund, D. Shear-strength Characteristics of A Residual Soil. *Can. Geotech. J.* **1995**, *32*, 60–77. [\[CrossRef\]](#)
- Anderson, S.A.; Sitar, N. Analysis of Rainfall-induced Debris Flows. *J. Geotech. Eng.* **1995**, *121*, 544–552. [\[CrossRef\]](#)
- Huang, C.C.; Yuin, S.C. Experimental Investigation of Rainfall Criteria for Shallow Slope Failures. *Geomorphology* **2010**, *120*, 326–338. [\[CrossRef\]](#)
- Sorbino, G.; Nicotera, M.V. Unsaturated Soil Mechanics in Rainfall-induced Flow Landslides. *Eng. Geol.* **2013**, *165*, 105–132. [\[CrossRef\]](#)
- Wen, B.P.; He, L. Influence of Lixiviation by Irrigation Water on Residual Shear Strength of Weathered Red Mudstone in Northwest China: Implication for Its Role in Landslides' Reactivation. *Eng. Geol.* **2012**, *151*, 56–63. [\[CrossRef\]](#)
- Dunne, T. Formation and Controls of Channel Networks. *Prog. Phys. Geogr.* **1980**, *4*, 211–239. [\[CrossRef\]](#)
- Higgins, C.G. Drainage Systems Developed by Sapping on Earth and Mars. *Geology* **1982**, *10*, 147–152. [\[CrossRef\]](#)
- Howard, A.D.; Mclane, C.F. Erosion of Cohesionless Sediment by Groundwater Seepage. *Water Resour. Res.* **1988**, *24*, 1659–1674. [\[CrossRef\]](#)
- Godt, J.W.; Coe, J.A. Alpine Debris Flows Triggered by a 28 July 1999 Thunderstorm in the Central Front Range, Colorado. *Geomorphology* **2007**, *84*, 80–97. [\[CrossRef\]](#)
- Lu, N.; Godt, J. Infinite Slope Stability under Steady Unsaturated Seepage Conditions. *Water Resour. Res.* **2008**, *44*, 2276–2283. [\[CrossRef\]](#)
- Khalili, N.; Geiser, F.; Blight, G.E. Effective Stress in Unsaturated Soils: Review with New Evidence. *Int. J. Geomech.* **2004**, *4*, 115–126. [\[CrossRef\]](#)
- Lu, N.; Likos, W.J. Suction Stress Characteristic Curve for Unsaturated Soil. *J. Geotech. Geoenviron. Eng.* **2006**, *132*, 131–142. [\[CrossRef\]](#)
- Rahardjo, H.; Ong, T.H.; Rezaur, R.B.; Leong, E.C. Factors Controlling Instability of Homogeneous Soil Slopes under Rainfall. *J. Geotech. Geoenviron. Eng.* **2007**, *133*, 1532–1543. [\[CrossRef\]](#)

26. Rahimi, A.; Rahardjo, H.; Leong, E.C. Effect of Hydraulic Properties of Soil on Rainfall-induced Slope Failure. *Eng. Geol.* **2010**, *114*, 135–143. [[CrossRef](#)]
27. Gui, M.W.; Wu, Y.M. Failure of Soil under Water Infiltration Condition. *Eng. Geol.* **2014**, *181*, 124–141. [[CrossRef](#)]
28. Rosenberry, D.O.; Pitlick, J. Local-scale Variability of Seepage and Hydraulic Conductivity in a Shallow Gravel-bed River. *Hydrol. Process.* **2009**, *23*, 3306–3318. [[CrossRef](#)]
29. Hatch, C.E.; Fisher, A.T.; Ruehl, C.R.; Stemler, G. Spatial and Temporal Variations in Streambed Hydraulic Conductivity Quantified with Time-series Thermal Methods. *J. Hydrol.* **2010**, *389*, 276–288. [[CrossRef](#)]
30. Mutiti, S.; Levy, J. Using Temperature Modeling to Investigate the Temporal Variability of Riverbed Hydraulic Conductivity during Storm Events. *J. Hydrol.* **2010**, *388*, 321–334. [[CrossRef](#)]
31. Briggs, M.A.; Lautz, L.K.; McKenzie, J.M.; Gordon, R.P.; Hare, D.K. Using High-resolution Distributed Temperature Sensing to Quantify Spatial and Temporal Variability in Vertical Hyporheic Flux. *Water Resour. Res.* **2012**, *48*, 72–84. [[CrossRef](#)]
32. Deljouei, A.; Cislighi, A.; Abdi, E.; Borz, S.A.; Majnounian, B.; Hales, T.C. Implications of hornbeam and beech root systems on slope stability: From field and laboratory measurements to modelling methods. *Plant Soil* **2022**, *483*, 547–572. [[CrossRef](#)]
33. Karimi, Z.; Abdi, E.; Deljouei, A.; Cislighi, A.; Shirvany, A.; Schwarz, M.; Hales, T.C. Vegetation-induced soil stabilization in coastal area: An example from a natural mangrove forest. *Catena* **2022**, *216*, 106410. [[CrossRef](#)]
34. Palazzolo, N.; Peres, D.J.; Creaco, E.; Cancelliere, A. Using principal component analysis to incorporate multi-layer soil moisture information in hydrometeorological thresholds for landslide prediction: An investigation based on ERA5-Land reanalysis data. *Nat. Hazards Earth Syst. Sci.* **2023**, *23*, 279–291. [[CrossRef](#)]
35. Uwihirwe, J.; Riveros, A.; Wanjala, H.; Schellekens, J.; Sperna Weiland, F.; Hrachowitz, M.; Bogaard, T.A. Potential of satellite-derived hydro-meteorological information for landslide initiation thresholds in Rwanda. *Nat. Hazards Earth Syst. Sci.* **2022**, *22*, 3641–3661. [[CrossRef](#)]
36. Wicki, A.; Lehmann, P.; Hauck, C.; Seneviratne, S.I.; Waldner, P.; Stähli, M. Assessing the potential of soil moisture measurements for regional landslide early warning. *Landslides* **2020**, *17*, 1881–1896. [[CrossRef](#)]
37. Bordoni, M.; Vivaldi, V.; Ciabatta, L.; Brocca, L.; Meisina, C. Temporal prediction of shallow landslides exploiting soil saturation degree derived by ERA5-Land products. *Bull. Eng. Geol. Environ.* **2023**, *82*, 308. [[CrossRef](#)]
38. Conte, E.; Pugliese, L.; Troncone, A. A Simple Method for Predicting Rainfall-Induced Shallow Landslides. *J. Geotech. Geoenviron. Eng.* **2022**, *148*, 04022079. [[CrossRef](#)]
39. Tinjum, J.M.; Benson, C.H.; Blotz, L.R. Soil-water Characteristic Curves for Compacted Clays. *J. Geotech. Geoenviron. Eng.* **1997**, *123*, 1060–1069. [[CrossRef](#)]
40. Ng, C.W.; Pang, Y.; Leung, A.; Zhou, C.; Yuan, Q.; Xu, J.; Chiu, C.; Yung, S.Y.; Sun, D.; Sheng, D.; et al. Experimental Investigations of the Soil-water Characteristics of Volcanic Soil. *Can. Geotech. J.* **2011**, *37*, 1252–1264. [[CrossRef](#)]
41. Ng, C.W.W.; Pang, Y.W. Influence of Stress State on Soil-water Characteristics and Slope Stability. *J. Geotech. Geoenviron. Eng.* **2000**, *126*, 157–166. [[CrossRef](#)]
42. Suits, L.D.; Sheahan, T.; Leong, E.; Tripathy, S.; Rahardjo, H. A Modified Pressure Plate Apparatus. *Geotech. Test. J.* **2004**, *27*, 322–331. [[CrossRef](#)]
43. Suits, L.D.; Sheahan, T.; Wang, X.; Benson, C. Leak-free Pressure Plate Extractor for Measuring the Soil Water Characteristic Curve. *Geotech. Test. J.* **2004**, *27*, 163–172. [[CrossRef](#)]
44. Niu, G.; Sun, D.; Wei, C.; Yan, R.; He, J.; Yu, M. Water Retention Behaviour of Complete-intense Weathering Mudstone and its Prediction. *Chin. J. Geotech. Eng.* **2016**, *38* (Suppl. 2), 216–221. (In Chinese)
45. Song, C.; Chai, S.X.; Wang, P. *The Soil Test and Test Analysis*; Tianjin University Press: Tianjin, China, 2007. (In Chinese)
46. Genuchten, M.T.V. A Closed-form Equation for Predicting the Hydraulic Conductivity of Unsaturated Soil. *Soil Sci. Soc. Am. J.* **1980**, *44*, 892–898. [[CrossRef](#)]
47. Fredlund, D.G.; Xing, A. Equations for the Soil-water Characteristic Curve. *Can. Geotech. J.* **1994**, *31*, 521–532. [[CrossRef](#)]
48. Vanapalli, S.K.; Fredlund, D.G.; Pufahl, D.E.; Clifton, A.W. Model for the Prediction of Shear Strength with Respect to Soil Suction. *Can. Geotech. J.* **1996**, *33*, 379–392. [[CrossRef](#)]
49. Fredlund, D.G.; Xing, A.; Fredlund, M.D.; Barbour, S.L. The Relationship of the Unsaturated Soil Shear to the Soil-water Characteristic Curve. *Can. Geotech. J.* **1996**, *33*, 440–448. [[CrossRef](#)]
50. Çokça, E.; Tilgen, H.P. Shear Strength-suction Relationship of Compacted Ankara Clay. *Appl. Clay Sci.* **2010**, *49*, 400–404. [[CrossRef](#)]

Disclaimer/Publisher’s Note: The statements, opinions and data contained in all publications are solely those of the individual author(s) and contributor(s) and not of MDPI and/or the editor(s). MDPI and/or the editor(s) disclaim responsibility for any injury to people or property resulting from any ideas, methods, instructions or products referred to in the content.